Imaging Magma Transport During the 1997 Seismic Swarm off the Izu Peninsula, Japan

Yosuke Aoki,[1,2] Paul Segall,[1] Teruyuki Kato,[2] Peter Cervelli,[1] Seiichi Shimada[3]

The spatio-temporal evolution of a propagating magma-filled crack was estimated from inversion of Global Positioning System (GPS) data, tiltmeters, and leveling. The dike opened at a maximum rate of 50 millimeters per day and had a peak magma flux of 2×10^6 cubic meters per day. Although the spatial resolution was limited, slow upward propagation was resolved during the 9-day-long intrusion. In contrast, the earthquakes migrated rapidly upward during the first 12 hours of the swarm, and nearly all of the seismic energy was released in the first 2 days. Comparison of inversion results with accurate hypocenter locations will lead to improved understanding of magma transport through the brittle crust and of the causes of volcanic seismicity.

Volcanoes often deform before erupting (*1*–*3*). Surface deformation measurements can be used to constrain the size, shape, and time-dependent evolution of magma bodies. Okada and Yamamoto (*2*) and Linde *et al*. (*3*) used strain, tilt, electronic distance, and GPS measurements to model the upward propagation of magma-filled cracks (dikes). These studies used forward-modeling techniques, rather than inversion, and would be difficult to extend to real-time forecasting. We used the network inversion filter (*4*) to invert for the spatial and temporal evolution of an intruding dike. This approach can potentially be extended to near–real-time monitoring, leading to improved eruption forecasting.

The Izu Peninsula, located in central Japan, has been the source of more than a dozen seismic swarms since 1978. The earthquakes are believed to be related to volcanic activity (*5*); indeed, the 1989 swarm led to a submarine eruption (*2*, *6*). On 2 March 1997 at 15:00 (GMT), a seismic swarm began offshore (Fig. 1). Focal depths decreased from 10 km to about 5 km in the first 12 hours of the swarm (Fig. 2). Nearly 80% of the seismic moment release occurred during the first 2 days of the swarm (*7*), and there was virtually no moment release after 9 March (Fig. 2).

GPS observations from permanent stations showed ~120 mm of NE-SW extension between stations 5105 and 3048 (Fig. 1). Leveling revealed uplift of nearly 30 mm, and continuously recording borehole tiltmeters showed a maximum of 13 μrad of NW tilt recorded at KWN (Fig. 1). In contrast to the short duration of the seismic moment release, the GPS and tilt measurements recorded deformation lasting as long as 10 days (Fig. 3). The temporal and spatial resolution of these data allowed us to invert for the growth of the dike in space and time and to compare the aseismic moment history with the moment released in the earthquake swarm.

As a preliminary step, we used a simulated annealing (*8*) algorithm to find the dike geometry (length, width, depth, dip, strike, and source location) that best fit the cumulative displacements and tilts spanning a 28-day interval including the deformation episode (*9*). The dike was approximated by a uniform opening, rectangular dislocation in a homogeneous, isotropic, elastic half-space. The best-fitting dike strikes NW-SE, which is consistent with the

[1]Department of Geophysics, Stanford University, Stanford, CA 94305–2215, USA. [2]Earthquake Research Institute, University of Tokyo, 1–1, Yayoi 1, Bunkyo-ku, Tokyo 113–0032, Japan. [3]National Research Institute for Earth Science and Disaster Prevention, 3–1, Tenno-dai, Tsukuba, Ibaraki 305–0006, Japan.

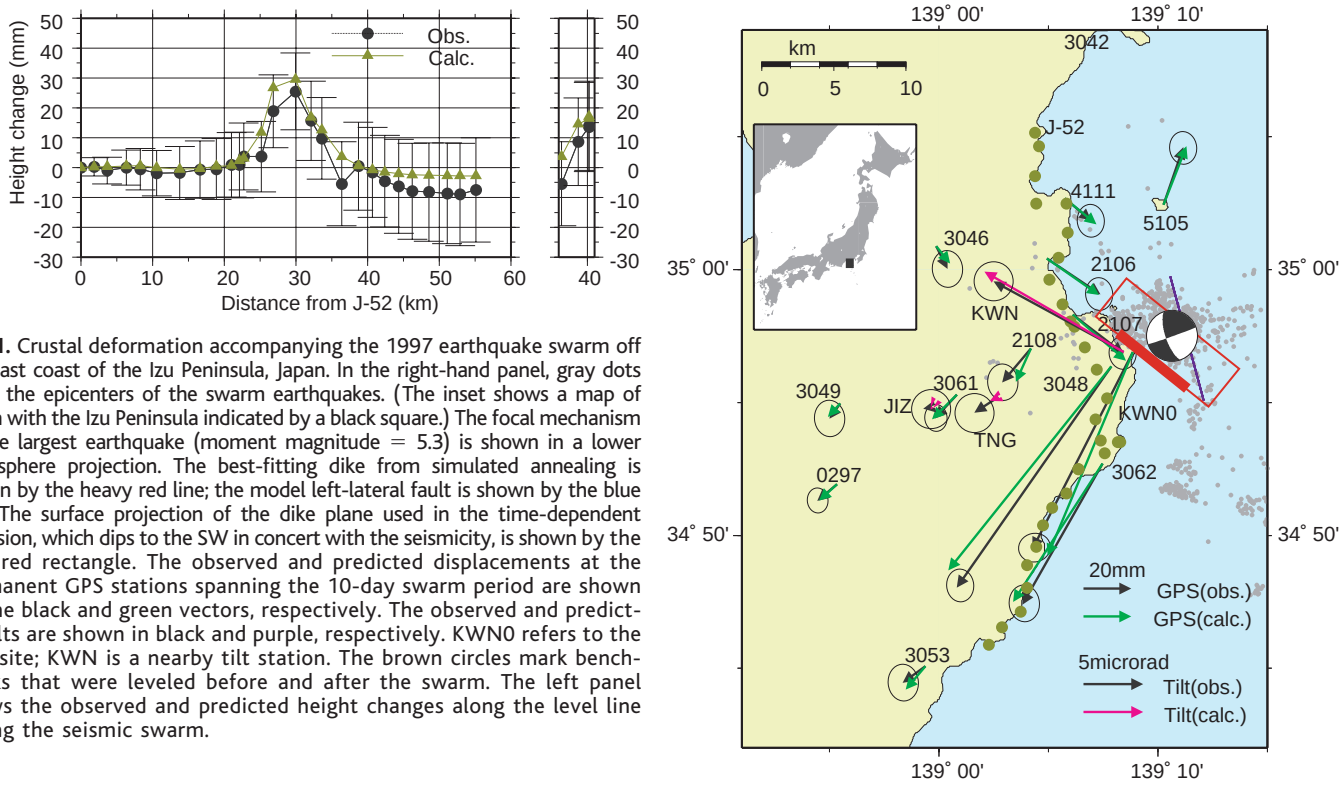

Fig. 1. Crustal deformation accompanying the 1997 earthquake swarm off the east coast of the Izu Peninsula, Japan. In the right-hand panel, gray dots mark the epicenters of the swarm earthquakes. (The inset shows a map of Japan with the Izu Peninsula indicated by a black square.) The focal mechanism of the largest earthquake (moment magnitude = 5.3) is shown in a lower hemisphere projection. The best-fitting dike from simulated annealing is shown by the heavy red line; the model left-lateral fault is shown by the blue line. The surface projection of the dike plane used in the time-dependent inversion, which dips to the SW in concert with the seismicity, is shown by the thin red rectangle. The observed and predicted displacements at the permanent GPS stations spanning the 10-day swarm period are shown by the black and green vectors, respectively. The observed and predicted tilts are shown in black and purple, respectively. KWN0 refers to the GPS site; KWN is a nearby tilt station. The brown circles mark benchmarks that were leveled before and after the swarm. The left panel shows the observed and predicted height changes along the level line during the seismic swarm.

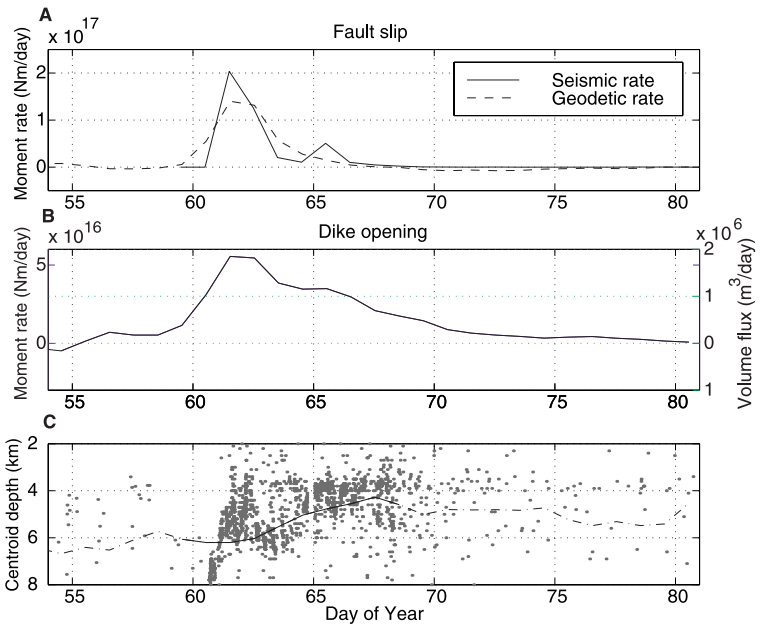

Fig. 2. Characteristics of the estimated model. (**A**) Moment release rate on the model left-lateral fault estimated from the inversion (dashed line) as compared to the seismic moment release rate (solid line), computed with a standard moment magnitude relation. (**B**) Moment rate of the dike intrusion and volume flux, showing that the intrusion lasted considerably longer than the energetic phase of the seismic swarm. The dike moment is the shear modulus, 30 GPa, times the dike volume. (**C**) Centroid depth of the dike as a function of time, dashed where the moment rate is low. Black circles show the depths of the swarm earthquakes.

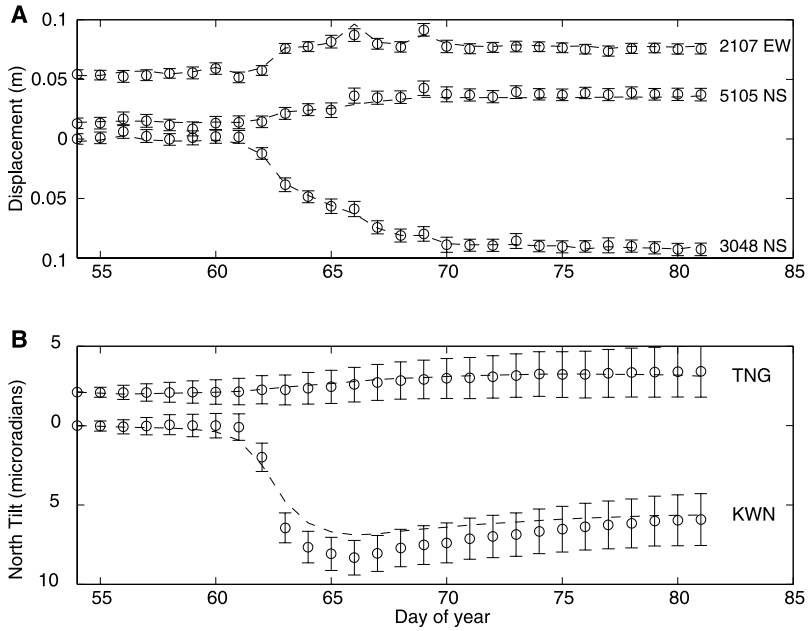

Fig. 3. (**A**) Comparison between observed and predicted GPS displacements (EW refers to east-west component, NS to north-south), relative to station 3042, and (**B**) tilt values. Observations are shown by circles with 1σ error bars. The prediction of the time-dependent inversion is shown by the dashed lines. Positive tilts are down to the south. The observed and predicted curves may be offset vertically (by the same amount) to avoid overlap with other stations. There is an abrupt offset in the EW component of station 2107 between DOY 62 and DOY 63 that is due to the largest earthquake, in contrast to the slow change in the NS component of station 3048, which is due to dike intrusion.

regional stress field (*10*) and previous forward-modeling studies of the 1989 intrusion and eruption (*2*). The dike model fit the SW-NE extension visible in the GPS data but could not explain the SE-directed motion at GPS sites 4111, 2106, and 2107. The data can be fit, however, when the simulated annealing includes two sources (Fig. 1). The second source is a vertical, left-lateral fault with strike consistent with the focal mechanism of the largest earthquake (Fig. 1). The fault is 8.9 km long, extends from a depth of 5.8 to 1.2 km, and involves 0.46 m of left-lateral slip. The dike is 5.6 km long, extends from a depth of 0.3 to 5.2 km, and opens 0.31 m.

The modeled dike (heavy red line in Fig. 1) is slightly offset to the SW of the swarm epicenters (gray dots in Fig. 1), which dip 70° to the southwest. Confidence intervals in the dike position and dip, determined by bootstrap resampling (*11*), suggest that the apparent offset between the dike and the swarm hypocenters is not significant at the 95% confidence level (*9*). Non-uniform elastic properties could also bias the estimated dike and fault geometry (*12*). Given the lack of offshore geodetic coverage, we adjusted the dip of the dike to agree with the earthquake distribution (*13*).

Next we estimated the spatial and temporal evolution of dike opening and fault slip using a network inversion filter (*4*). The dike and fault planes were extended 40% laterally and vertically to allow for spatial variations in dike opening. The data consist of 28 daily GPS position determinations and 24-hour averaged tilts beginning on 23 February 1997. The two leveling surveys span the entire swarm episode and help constrain the total amount of deformation, but not its temporal evolution. Errors in the observations, including frequency-dependent noise in the tilt data, were accounted for in the inversion (*14*).

Dike opening and fault slip were expanded in spatial basis functions chosen to minimize the roughness of the opening distribution as measured by $\|\nabla^2 s(\mathbf{x})\|$, where $s(\mathbf{x})$ is the opening on the dike plane (or fault slip), and ∇^2 is a finite difference approximation to the Laplacian operator (*15*). A weighted singular value decomposition of the data kernel yields an orthogonal basis (*4*), of which the first eight terms were included in the representation of the dike opening and fault slip, for a total of 16 basis functions. The estimated distributions depend on spatial and temporal smoothing parameters, which were chosen to optimize the fit to the data without causing the estimated dike opening or fault slip to become unnecessarily complex (*16*). Solutions with our preferred values of the spatial and temporal smoothing parameters are consistent with the GPS and tilt time histories (Fig. 3).

Dike injection began on DOY (day of the year) 61, 2 March, simultaneously with the onset of the seismic swarm (Fig. 4). The rate of dike opening peaked on DOY 62 and 63 and continued until DOY 69 (*17*). The cumulative dike dilation (not shown in Fig. 4) reached a maximum of 0.38 m. Despite the fact that we have approximated the spatially distributed earthquakes with a single plane and ignored spatial variations in rock properties, the rate of left-lateral faulting computed from the geodetic

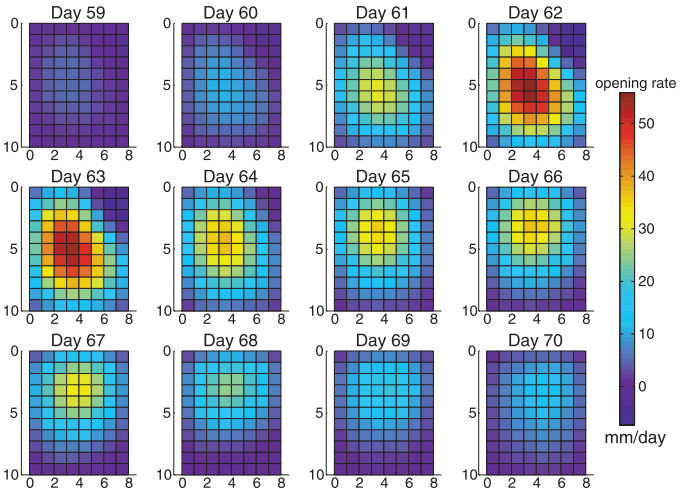

Fig. 4. Temporal and spatial distribution of dike opening from the time-dependent inversion. Each panel represents the dike plane, viewed from the southwest, with depth in kilometers along the vertical axis, and along-strike distance in kilometers along the horizontal axis. The color represents the rate of dike opening, measured in millimeters per day. Each panel represents the opening rate for 1 day.

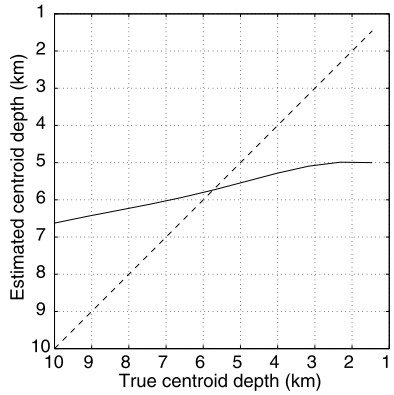

Fig. 5. Estimated centroid depth for a single patch of dike opening 0.9 km deep by 1 km wide, located at the given true depth in the center of the dike plane. We estimated the spatial resolution by conducting a time-independent inversion using the cumulative displacements and tilts from the beginning to the end of the episode. A linear combination of the data misfit and the solution roughness $r^T\Sigma^{-1}r + \lambda^2\|\nabla^2 s(\mathbf{x})\|$ was minimized, where r is the residual vector, T indicates transpose, Σ is the data covariance, and λ is a damping parameter. λ was chosen so that the spatial roughness and maximum opening matched the output of the network inversion filter. The resolution matrix R was computed from $s_{est} = Rs$, where s_{est} is the estimated dike opening. The centroid of s_{est} is shown as a function of the true source depth. The estimated upward propagation underestimates the true rate by about a factor of 2.

and tilt data agrees with the moment released by the swarm of earthquakes (Fig. 2A). The estimated geodetic moment release on the fault before DOY 61 is probably an artifact of temporal smoothing in the inversion method. The results show that the dike intrusion lasted longer than the 2 days of significant seismic moment release (Fig. 2B). The inferred magma flux peaked on DOY 62–63 at $\sim 2 \times 10^6$ m^3/day.

The area of maximum dike opening became shallower with time (Fig. 4). We quantified this by computing the centroid depth (*18*) of the opening-rate distribution. The centroid depth shallows from ~6 to ~4 km between DOY 61 and DOY 67 (Fig. 2C). This is a conservative estimate, because the spatial smoothing tends to shift the opening to the middle of the dike plane. The inversion may underestimate the true upward migration of the dike opening by a factor of 2 (Fig. 5). In all of the inversions we investigated, the centroid depth shallows during the phase of significant dike opening. The upward migration is controlled by the tilt data from station KWN, which reverses sign after DOY 66. For a vertical dike in an elastic body, there is subsidence above the dike and uplift on the flanks. Thus, a rising dike causes tilt first toward and then away from the dike (*19*). This pattern has been seen at KWN during many swarm episodes (*20*), giving us confidence that the signal is real.

Near–real-time implementation of the methods described here could allow for improved forecasts of volcanic hazards. It should be possible to image some dikes as they propagate, provided some aspects of the source geometry are known a priori or can be rapidly estimated. For example, rift zones of Hawaiian and Icelandic volcanoes are known loci of eruptive activity. Such an approach could lead to improved forecasts of the size and location of potential eruptions. Further work is needed to predict whether a given dike will arrest before breaching the surface or will actually lead to an eruption.

It is generally believed that swarms of earthquakes occur because of stress concentrations near the dike tip (*21*). This would imply that the migration of seismicity faithfully records the evolution of the dike. However, by using deformation measurements, we found that the dike propagated vertically on a time scale of several days, whereas the earthquakes migrated on a time scale of 12 hours. In addition, the seismic moment release was much shorter in duration than was the dike opening (Fig. 2A). It is possible that the pulse of seismic energy release reflects triggering of stored elastic strain energy by stress perturbations due to dike growth. Relative tension above the dike tip, normal to the dike plane, would favor left-lateral faulting, as observed in the focal mechanisms. If the ambient stress state was sufficiently close to failure, stress changes due to dilation of a slowly propagating, or even static, dike could trigger earthquakes over a broad area. The rate at which a critical stress state migrates away from the dike depends on the rate of dike opening and the vertical profile of the dike-induced stresses. High-resolution earthquake locations (*22*) compared with geodetic inversions of the type presented here will lead to a better understanding of magma transport through the brittle crust and the causes of volcanic seismicity.

References and Notes

1. J. J. Dvorak and D. Dzurisin, *Rev. Geophys.* **35**, 343 (1997).
2. Y. Okada and E. Yamamoto, *J. Geophys. Res.* **96**, 10361 (1991).
3. A. T. Linde, K. Agustsson, I. S. Sacks, R. Stefansson, *Nature* **365**, 737 (1993).
4. P. Segall and M. Matthews, *J. Geophys. Res.* **102**, 22391 (1997).
5. M. Ishida, *Bull. Seismol. Soc. Am.* **74**, 199 (1984).
6. S. Shimada *et al.*, *Nature* **343**, 631 (1990).
7. Earthquake Research Institute, "Seismic activities in the Izu Penninsula and its vicinity" (in Japanese), *Rep. Coord. Comm. Earthquake Predict.* **58**, 239 (1997).
8. A. Basu and L. N. Frazer, *Science* **249**, 1409 (1990).
9. P. Cervelli, M. H. Murray, P. Segall, Y. Aoki, T. Kato, in preparation.
10. M. Ukawa, *J. Geophys. Res.* **96**, 713 (1991).
11. B. Efron and R. Tibshirani, *An Introduction to the Bootstrap* (Chapman & Hall, New York, 1993).
12. Y. Du, P. Segall, H. Gao, *Geophys. Res. Lett.* **24**, 2347 (1997); J. C. Savage, *J. Geophys. Res.* **103**, 2439 (1998).
13. With a dip of 70° and the bottom edge of the dike fixed at the simulated annealing result, the modeled dike agrees with the earthquake distribution. The time-dependent inversion results were not changed significantly if we assumed a vertical dike offset 1.4 km to the NE of the simulated annealing result. The best-fitting dike from simulated annealing is almost immediately below station KWN0. Because there is no tilt predicted above a vertical dike, this geometry requires large shallow opening in order to fit the tilt data.
14. Errors in the GPS positions were determined by scaling the formal covariance matrices to be consistent with the repeatability in a 30-day period well after the swarm had ended. Frequency-dependent noise in the GPS data, although included, was not significant on the time scale of 30 days. Noise in the tilt was assessed from 1 year of data, not perturbed by swarm activity. We estimated a random walk error of 3 μrad/$\sqrt{\text{year}}$ and a frequency independent error of 10 nrad. Finally, circuit misclosures indicated leveling errors of 1.2 mm/$\sqrt{\text{km}}$.
15. R. Harris and P. Segall, *J. Geophys. Res.* **92**, 7945 (1987).
16. The spatial and temporal smoothing parameters are denoted γ and α, respectively. Increasing γ improves the fit to the data at the expense of increasing the spatial roughness of the dike opening and fault slip. We found that values of γ greater than 5 did not improve the fit to the data significantly but caused the cumulative dike opening to be locally negative (dike closing). We therefore used $\gamma = 5$ in the final solutions. In the temporal domain, $\alpha = 0$ corresponds to steady-state behavior. Increasing α improves the fit to the data, at the expense of increasing the temporal complexity of the model. For these data, we found that the likelihood (4) did not increase substantially for α greater than 1000, so $\alpha = 1000$ was used in the final solutions. Much smaller values of α do not fit the tilt data; for much larger values, the solution tends to fit day-to-day scatter in the GPS displacements.

17. An animation of the dike can be viewed at http://pangea.stanford.edu/~segall/izu.html.
18. The centroid depth is the average depth weighted by the magnitude of the dike opening.
19. D. D. Pollard, P. Delaney, W. A. Duffield, E. T. Endo, A. T. Okamura, *Tectonophysics* **94**, 541 (1983).
20. Y. Okada, E. Yamamoto, T. Ohkubo, in preparation.
21. A. M. Rubin and D. Gillard, *J. Geophys. Res.* **103**, 10017 (1998).
22. D. Gillard, A. M. Rubin, P. Okubo, *Nature* **384**, 343 (1996); D. P. Schaff, G. Beroza, B. E. Shaw, *Geophys. Res. Lett.* **25**, 4549 (1998).
23. We thank the Geographical Survey Institute of Japan and the National Research Institute for Earth Science and Disaster Prevention of Japan for access to data and P. Delaney, Y. Okada, B. Ellsworth, G. Beroza, T. Dixon, and an anonymous reviewer for helpful comments. Supported by a grant from NASA's Solid Earth and Natural Hazards program to Stanford University.

15 July 1999; accepted 27 September 1999

Abrupt Climate Change at the End of the Last Glacial Period Inferred from Trapped Air in Polar Ice

Jeffrey P. Severinghaus[1] and Edward J. Brook[2]

The last glacial period was terminated by an abrupt warming event in the North Atlantic ~15,000 years before the present, and warming events of similar age have been reported from low latitudes. Understanding the mechanism of this termination requires that the precise relative timing of abrupt climate warming in the tropics versus the North Atlantic be known. Nitrogen and argon isotopes in trapped air in Greenland ice show that the Greenland Summit warmed 9 ± 3°C over a period of several decades, beginning 14,672 years ago. Atmospheric methane concentrations rose abruptly over a ~50-year period and began their increase 20 to 30 years after the onset of the abrupt Greenland warming. These data suggest that tropical climate became warmer or wetter (or both) ~20 to 80 years after the onset of Greenland warming, supporting a North Atlantic rather than a tropical trigger for the climate event.

Evidence for extremely abrupt changes in Earth's climate has come principally from the annually layered Greenland ice cores (*1*–*7*), although the tropics collect most solar radiation and are central to Earth's heat and water vapor budgets (*8*). Accordingly, tropical climate records are critical for understanding abrupt climate events. Especially important are those records that reveal cause-and-effect relations by giving the precise relative timing of changes in the tropics and the high latitudes. However, high-resolution tropical climate records are few in number and for the most part equivocal on the existence and timing of abrupt climate events.

Evidence from Bolivian ice cores at 18°S shows that tropical climates warmed rapidly about 15 thousand years (ky) B.P. (before present, where present is 1950 A.D.) (*9*). This warming is roughly synchronous with prominent warming at 14.67 ky B.P., known as the Bølling Transition, seen in the Greenland Summit ice cores (*1*, *2*, *5*), European pollen records (*10*), and many North Atlantic sediment records (*11*, *12*). Other recent studies have documented low-latitude rapid climate shifts at about this time in the Santa Barbara basin (*13*), Arabian Sea (*14*), and the Cariaco basin of Venezuela (*15*); however, dating uncertainties of a century or more limit the precision with which the timing of these events and their putative Arctic counterpart may be compared.

Atmospheric methane concentrations also increased abruptly at this time, as inferred from measurements of trapped air bubbles in the Greenland Summit ice cores (*16*, *17*) and Antarctic ice cores (*18*, *19*). This increase is thought to have been caused by an increase in wetland extent and temperature, as wetlands were the principal source of methane in the preindustrial period (*17*) and changes in sink strength are thought to have been small (*20*). Tropical wetlands have been proposed as a major contributor to the Bølling methane increase, because ice sheets covered the primary extratropical methane source areas at this time (*17*, *21*). This hypothesis is supported by the fact that the difference between Greenland and Antarctic methane concentrations (referred to as the interpolar gradient) underwent a relatively small increase despite the ~25% jump in concentration (*21*, *22*). When inverted for source distribution with a three-box atmospheric transport model, methane records from Greenland and Antarctica imply a predominantly low-latitude source (*23*). Because the atmosphere is well mixed (mixing time of ~1 year) relative to methane's lifetime in the atmosphere (~10 years) (*24*) and wetland methane emissions are broadly correlated with temperature and precipitation, methane concentration integrates climate information over the entire tropical region. Knowledge of the precise timing of the abrupt methane increase relative to the Greenland warming should thus place constraints on the relative timing of tropical and Arctic abrupt climate change.

Two problems have prevented relating changes in temperature and methane in the ice core record. First, the age of the air trapped in bubbles is less than the age of the enclosing ice because air is occluded at some depth below the surface of the ice sheet in the bubble close-off region (*25*, *26*). This gas age–ice age difference is not known well for past times, making uncertain the relative timing of temperature (which is obtained from the ice matrix) and atmospheric gas changes (*17*, *26*). Second, the temperature inferred from the $^{18}O/^{16}O$ ratio of the ice ($\delta^{18}O_{ice}$) is uncertain because factors other than local mean annual temperature may affect this ratio, such as the seasonality of precipitation at the ice core site (*27*) and the temperature and proximity of the water vapor source (*28*, *29*). Borehole temperature calibrations of the $\delta^{18}O_{ice}$ paleothermometer have demonstrated that the modern spatial calibration underestimates the glacial cooling by a factor of two (*30*). These issues have raised the question of whether the abrupt increases in Greenland $\delta^{18}O_{ice}$ represent isotopic artifacts rather than local temperature changes as commonly inferred (*29*, *31*) and have created uncertainty about the magnitude of temperature change they may indicate.

Here we address these problems with measurements of isotopes of nitrogen and argon gas trapped in air bubbles in the GISP2 (Greenland Ice Sheet Project 2) ice core. Bubble $^{15}N/^{14}N$ and $^{40}Ar/^{36}Ar$ record a signal of rapid temperature change at the surface of the ice sheet (*7*). The combination of nitrogen and argon isotope measurements provides a direct estimate of the magnitude of the temperature increase, based on laboratory calibration of the isotope fractionation due to thermal diffusion. Methane and nitrogen diffuse downward through the snow layer at nearly the same speed (*32*) and are trapped together in the bubbles, making a precise comparison of the timing of atmospheric methane change and local temperature change possible (*7*).

The porous and partially consolidated layer of snow on top of polar ice sheets (known as firn) contains air that mixes by molecular diffusion with the overlying atmosphere (*25*). The isotopes of gases in this stagnant column of air

[1]Scripps Institution of Oceanography, University of California, San Diego, 9500 Gilman Drive, La Jolla, CA 92037, USA. E-mail: jseveringhaus@ucsd.edu [2]Department of Geology, Washington State University, 14204 NE Salmon Creek Avenue, Vancouver, WA 98686, USA. E-mail: brook@vancouver.wsu.edu